International Journal of Solids and Structures 49 (2012) 1045–1062

Contents lists available at SciVerse ScienceDirect

International Journal of Solids and Structures

journal homepage: www.elsevier.com/locate/ijsolstr

Comprehensive numerical analysis of a three-pass bead-in-slot weld and its critical validation using neutron and synchrotron diffraction residual stress measurements

O. Muránsky [a,*], M.C. Smith [b], P.J. Bendeich [a], T.M. Holden [c], V. Luzin [d], R.V. Martins [e], L. Edwards [a]

[a] ANSTO, Institute of Materials Engineering, New Illawarra Road, Lucas Heights, NSW, Australia
[b] EDF Energy, Barnett Way, Barnwood, Gloucester GL4 3RS, United Kingdom
[c] Northern Stress Technologies, Deep River, Ontario, Canada K0J 1P0
[d] ANSTO, Bragg Institute, New Illawarra Road, Lucas Heights, NSW, Australia
[e] Institute for Energy, Joint Research Centre, European Commission, Westerduinweg 3, 1755 LE Petten, The Netherlands

ARTICLE INFO

Article history:
Received 27 April 2011
Received in revised form 29 June 2011
Available online 22 July 2011

Keywords:
Finite element modelling
Residual stress
Neutron diffraction
Synchrotron diffraction
Welding process

ABSTRACT

The current paper presents a finite element simulation of the residual stress field associated with a three pass slot weld in an AISI 316LN austenitic stainless steel plate. The simulation is split into uncoupled thermal and mechanical analyses which enable a computationally less expensive solution. A dedicated welding heat source modelling tool is employed to calibrate the ellipsoidal Gaussian volumetric heat source by making use of extensive thermocouple measurements and metallographic analyses made during and after welding. The mechanical analysis employs the Lemaitre–Chaboche mixed hardening model. This captures the cyclic mechanical response which a material undergoes during the thermo-mechanical cycles imposed by the welding process. A close examination of the material behaviour at various locations in the sample during the welding process, clearly demonstrates the importance of defining the correct hardening and high temperature softening behaviour. The simulation is validated by two independent diffraction techniques. The well-established neutron diffraction technique and a very novel spiral slit X-ray synchrotron technique were used to measure the residual stress–strain field associated with the three-pass weld. The comparison between the model and the experiment reveals close agreement with no adjustable parameters and clearly validates the used modelling procedure.

1. Introduction

There is currently a strong interest in quantifying the stresses in welds used in the nuclear industry especially for nuclear power stations some of which have been in operation for more than two decades. In most cases it is impractical to perform residual stress measurements for every single weld in a welded structure. Additionally, the dimensions of real structural components are usually very large, hence non-destructive neutron and X-ray methods cannot be used simply because the path lengths and beam attenuation through the materials are too large (Hutchings et al., 2005). In such cases verified numerical methods may be the only method available for reliable determination of residual stress. It is, thus, important to establish the accuracy of the models for situations where critical comparisons may be made between model and experiment. A series of measurements on gradually more complex geometries have already been started under the auspices of the European network on Neutron Techniques Standardisation for Structural Integrity (NeT). The present sample is one of these series (NeT - Task Group 4, TG4) and is intended to predict and measure three-dimensional (3D) residual stresses associated with a three-pass austenitic slot weld in an AISI 316LN stainless steel plate.

The aim of numerical weld modelling is to develop models that are usable for control and design of welding processes in order to obtain appropriate mechanical performance of the welded component or whole structure (Lindgren, 2007). In recent years finite element (FE) simulations have become a very promising tool in predicting the residual stresses associated with a welded structure mainly due to ever-increasing computer power. Despite this, reliable prediction of residual stresses in a weld structure remains a difficult task because of the complexity of the welding process (Gilles et al., 2009) (Fig. 1(a) shows physical processes involved in the welding). It is a common practice to decrease the level of complexity by simplifying the geometry, reducing the dimension of the problem from 3D to 2D, and neglecting certain physical phenomena (i.e. heat transfer from the arc and droplets, the effect of

* Corresponding author. Tel.: +61 2 9717 3488; fax: +61 2 9543 7179.
E-mail address: ondrej.muransky@ansto.gov.au (O. Muránsky).

0020-7683/$ - see front matter Crown Copyright © 2011 Published by Elsevier Ltd. All rights reserved.
doi:10.1016/j.ijsolstr.2011.07.006

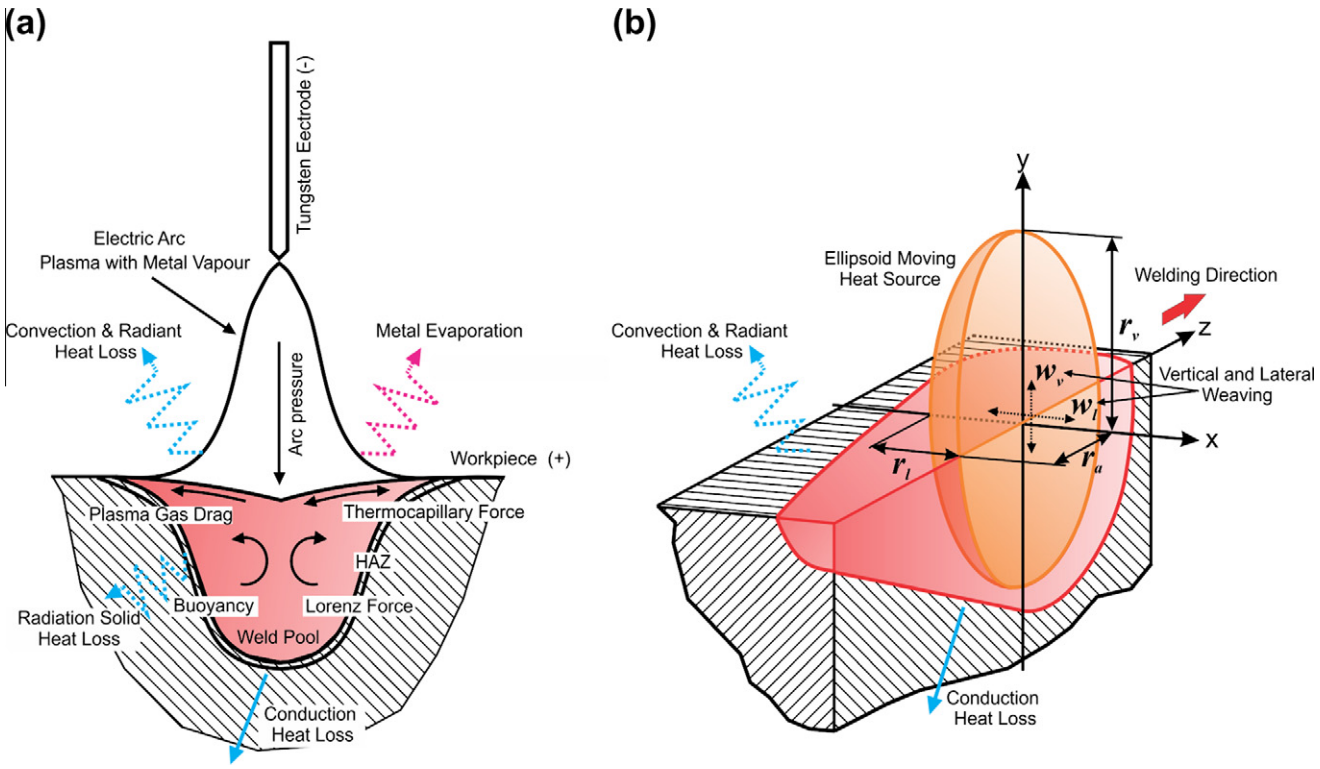

Fig. 1. (a) *Reality*: physical processes involved in welding process and driving forces in fluid flow in weld pool (Gilles et al., 2009). (b) *Model*: physical processes and simplified ellipsoid moving heat source included in the present finite element models.

arc pressure, metal evaporation, etc. Gilles et al., 2009). Additionally, temperature dependent material characteristic data is not trivial to obtain while it is shown to play a crucial role in predicting the final residual stresses within a welded structure. Although numerical models do not fully replace experimental methods, their main role is in understanding the welding process leading to fewer validation experiments needed to evaluate e.g. different design concepts (Lindgren, 2007).

The non-destructive determination of residual stress by neutron diffraction has been now available for more than thirty years. The standard procedures for making such measurements as well as the advantages and disadvantages of the neutron diffraction technique are summarized in Hutchings et al. (2005). Synchrotron X-ray based non-destructive methods became available in the last decade and new techniques are always emerging (Schreyer and Clemens, 2008). The spiral slit technique (Martins and Honkimäki, 2003) used in the current work is one of the very recent techniques which provides a number of advantages over classical neutron diffraction measurements, however it is still not commonly used. In general, all bulk diffraction-based measurements of residual stresses require knowledge of the lattice spacing of the material in the unstrained (stress-free) condition. One solution to this problem is to measure the lattice parameter in small cubes cut from the specimen, thereby assuming that the cubes are in a state of zero macroscopic stress. A well-known problem in case of diffraction based residual stress measurements in austenitic welds is grain growth in the weld. This leads to a situation where only a few grains ($\sim$10) are correctly oriented for diffraction leading to poor measurement statistics. This large grain situation is encountered in these experiments and leads to intrinsic limitations on the accuracy of the measurements as discussed later. Furthermore, grain growth occurs with ⟨001⟩ crystallographic directions aligned with the directions of heat flow out of the weld and this can create strong texture in the weld. This does not provide an intrinsic barrier to measurements but it may mean that the {hkl} reflection chosen for the measurements may be weak in some directions.

In the present paper FE modelling is employed in assessing the development of the residual stresses in a three-pass slot weld specimen in austenitic stainless steel (NeT – TG4 international benchmark specimen). An uncoupled thermal-mechanical FE simulation was carried out making the use of detailed welding parameters and thermocouple data recording during the welding process. A dedicated welding heat source modelling tool was used in order to reduce the uncertainties in the thermal solution by calibrating ellipsoidal Gaussian volumetric heat sources using the detailed welding records. The mechanical analysis employed the Lemaitre–Chaboche mixed isotropic-kinematic hardening model in order to produce the most representative material response to the cyclic thermo-mechanical loading imposed during welding. The neutron and synchrotron diffraction techniques were employed to validate (bench-mark) the current FE modelling procedure. The neutron diffraction method is well accepted for this purpose while the synchrotron spiral slit method used here offers a number of innovations including higher three dimensional spatial resolution which can be readily compared with the FE simulations.

2. Experimental specimen

2.1. Weld specimen

The weld was made in a 194 mm × 150 mm × 18 mm block of AISI 316LN stainless steel (chemical composition is shown in Table 1) with a slot 80 mm long and 6 mm deep. A photograph of the weld sample is shown in Fig. 2(a) including the specimen coordinate system. After machining the slot, but before welding, the piece was stress relieved by furnace-heating from room temperature to 1050 °C at 5 °C/min, held at 1050 ± 5 °C for 45 min, furnace-cooled to 300 °C and then air-cooled to room temperature.

Table 1
Chemical composition of the parent metal (AISI 316L) and filler material (ER316L).

	C	Cr	Ni	Si	Mn	Mo	Nb	N	P	S	Cu
AISI 316L [wt.%]	0.027	17.5	12.5	0.37	1.7	2.47	0.005	0.072	–	–	–
ER316L [wt.%]	0.02	19.04	12.20	0.49	1.84	2.1	–	–	0.018	0.001	0.05

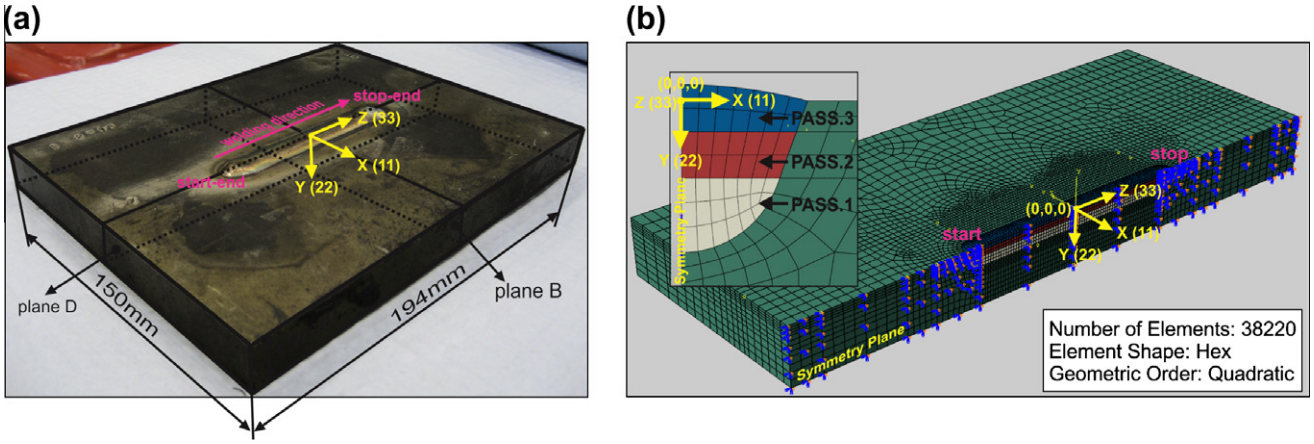

Fig. 2. (a) NeT – TG4 three-pass slot weld in an AISI 316LN stainless steel (international benchmark specimen). (b) The Abaqus half model depicting the basic plate geometry and three consecutive passes filling the slot. The insert shows in detail elements associated with passes 1 to 3.

Table 2
Defined welding parameters for all passes.

	Welding current [A]	Arc voltage [V]	Travel speed [mm/sec]	Heat input [J/mm]	Bead length [mm]	Energy [kJ]	Interpass temperature [°C]
PASS 1	220	10	1.27	1732	74*	128*	20 ± 10
PASS 2	195	10	1.27	1535	76*	117*	50 ± 10
PASS 3	185	10	1.27	1457	82	119	50 ± 10

* Bead lengths for passes 1 and 2 were estimated using a slot length in their positions.

The slot was then filled with three superimposed tungsten inert gas (TIG) weld passes. The welding parameters are shown in Table 2. ER316L filler wire with 0.9 mm diameter was used. The chemical composition of the filler material is shown in Table 1. Since the plate-parent and filler-weld materials remain austenitic throughout the whole welding process no solid-state phase transformation needs to be modelled. However, the higher Cr content in the filler material leads to stabilization of δ-ferrite, which ranges from 0 to 6 FN (ferrite number) (Brough, 1983; Vasudevan et al., 2003). The Rietveld diffraction pattern analysis collected on the high resolution diffractometer ECHIDNA at the OPAL reactor (Liss et al., 2006) confirmed ~5% δ-ferrite in the reference sample taken from the top of the weld. (Note that the presence of δ-ferrite was neglected in the stress analysis.)

The specimens were welded via mechanised TIG free of restraint so that the plate would distort without inhibition. The specimens distorted upon welding by bending along the line of the weld (Z-axis) by about ±0.8°, and also by bending about a line perpendicular to the weld (X-axis) by ~0.4° (Fig. 2). In total 12 samples were manufactured from which 7 were made available for round robin residual stress measurements in the NeT collaboration. Three of these specimens were extensively instrumented with a range of thermocouples at various locations in order to provide an input for the FE analysis. The present work discusses the measurement results obtained on two of the identically prepared round robin specimens: (i) the neutron diffraction measurements were made on a sample with reference number "2-1A" (one of the instrumented samples), and (ii) the synchrotron diffraction measurements were carried out on a sample with the identification number "3-1A".

2.2. Reference specimens

Reference specimens were EDM cut from a dedicated weld specimen from three different locations: (i) parent metal, (ii) top-weld metal, and (iii) bottom-weld metal (see Fig. 3). In order to eliminate macroscopic residual stresses but achieve a sufficiently large specimen volume for neutron diffraction measurements each reference specimen of 5 mm × 8 mm × 6 mm was assembled from four smaller cuboids with dimension of 4 mm × 3 mm × 5 mm. The reference specimen batch for the measurements by neutron diffraction carried the identification mark "X", and the batch used for the synchrotron X-ray diffraction measurements carried the identification mark "Z".

2.3. Microstructure

Micrographs revealed grain diameters between 30 and 60 μm in the plane perpendicular to the rolling direction and between 30 and 90 μm in the plane perpendicular to the plate normal direction (see micrographs in Fig. 3). In the weld metal it is difficult to recognize the grain boundaries, but one can clearly see in the insert of Fig. 3 an extended dendritic structure of the weld metal.

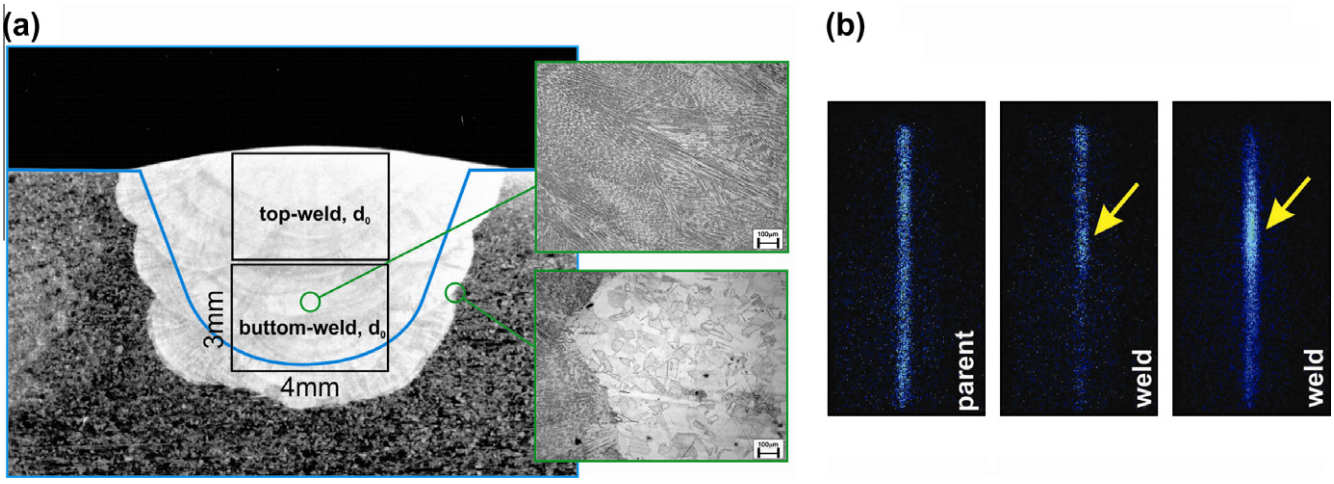

Fig. 3. (a) Macrograph showing the accumulated fusion zone of the three consecutive passes and a detail micrographs from the weld metal (top insert), and weld-parent metal interface (bottom insert). (b) 2D KOWARI detector image showing neutron diffraction distribution in parent (first image) and weld (second and third image) metal.

3. Finite element modelling

A 3D half model with 38220 Hex Quadratic elements and a symmetry plane on the weld centreline (Z-axis) was built using ABAQUS 6.9 CAE (ABAQUS, 2008), see Fig. 2(b). The insert in Fig. 2(b) shows elements associated with PASS.1, PASS.2, and PASS.3 at weld mid-length ($Z = 0$). The simulation was split into consecutive, uncoupled, thermal and mechanical analyses. It means that initially the thermal analysis solution was found and then the thermal solution (see Section 3.1) was imported into the mechanical analysis (see Section 3.2) via the "Predefined Field" interface in ABAQUS. Due to the fact that the plate (AISI 316LN) and filler (ER316L) material differ only in the Cr content the same thermal, thermo-physical and mechanical properties were used for the parent metal (plate) and weld metal in the current simulations. (Note that the weld metal is considered to be all material heated over 1400 °C.) All the material properties are summarized in the article appendix (Tables 4–7).

Table 4
Thermal properties of AISI 316LN stainless steel (parent metal) as a function of temperature, thermal conductivity (λ), and specific heat ($\mathbf{c}_p$).

T [°C]	λ [W m^{-1} °C^{-1}]	c_p [J kg^{-1} °C^{-1}]
20	0.01412	492
100	0.01526	502
200	0.01669	514
300	0.01811	526
400	0.01954	538
500	0.02096	550
600	0.02238	562
700	0.02381	575
800	0.02523	587
900	0.02666	599
1000	0.02808	611
1100	0.02950	623
1200	0.03093	635
1300	0.03235	647
1400	0.03278	659

3.1. Thermal modelling

The detailed record of the welding parameters during the welding process of all TG4 specimens and the data from an array of 12 thermocouples on three of the welded specimens provided an opportunity for developing an accurate pass-by-pass moving-heat-source simulation. The basic welding parameters for individual passes which were used to calibrate the welding heat source are tabulated in Table 2. Note that the torch traverse was stopped manually when the welding engineer judged it appropriate, hence this manual procedure led to a small variation in traverse length and total arc time between specimens.

The welding heat source was calibrated using a dedicated weld heat source modelling tool (FEAT-WMT) (Smith et al., 2009b). FEAT-WMT uses a steady state 3D moving mesh solution with a Gaussian ellipsoidal or Goldak heat source to calibrate the welding parameters against weld measured fusion zone and thermocouple measurements. The calibrated 3D moving heat source may be then used to derive an equivalent 2D heat source for use in 2D, axi-symmetric or 3D block-dumped analyses if the added complexity of a 3D moving heat source simulation is not required. Note that the 1400 °C isotherm (1375–1400 °C is the melting range of AISI 316L) corresponds closely to the weld fusion zone, so it can be readily compared with the fusion zone measured from a micrograph prepared by weld sectioning. FEAT-WMT generates weld-heat-flux time slice files for use in ABAQUS via the DFLUX user subroutine.

In the present simulations a simple ellipsoidal heat source was employed:

$$q = \frac{Q}{V_a}\exp - \left(\left(\frac{x}{r_l}\right)^2 + \left(\frac{y}{r_v}\right)^2 + \left(\frac{z}{r_a}\right)^2 \right), \quad (1)$$

Table 3
Optimal heat source parameters used in the modelling the moving torch.

	Optimal heat source ellipsoid parameters			Optimal heat source weave parameters		Efficiency [%]	Fusion area	
	A-radius [mm]	L-radius [mm]	V-radius [mm]	H-position [mm]	V-position [mm]		Measured [mm^2]	Predicted [%]
PASS 1	2.8	1.8	1.5	0.0–3.5	0.7–0.0	73	28.81	101% of measured
PASS 2	1.8	1.5	1.5	0.0–3.5	1.5–0.5	72	29.16	100% of measured
PASS 3	1.8	1.5	1.5	0.0–4.5	1.5–0.8	71	30.22	100% of measured

Table 5
Elastic mechanical properties of AISI 316LN stainless steel (parent metal) as a function of temperature, Young's modulus (**E**), and Poisson ratio (***v***).

T [°C]	AISI 316LN		
	E [MPa]	v	α [°C^{-1}]
20	195600	0.29	1.46E-05
100	191200	0.29	1.54E-05
200	185700	0.29	1.62E-05
300	179600	0.29	1.69E-05
400	172600	0.29	1.74E-05
500	164500	0.29	1.78E-05
600	155000	0.29	1.81E-05
700	144100	0.29	1.84E-05
800	131400	0.29	1.87E-05
900	116800	0.29	1.90E-05
1000	100000	0.29	1.93E-05
1100	80000	0.29	1.95E-05
1200	57000	0.29	1.98E-05
1300	30000	0.29	2.00E-05
1400	2000	0.29	2.02E-05

Table 6
Plastic mechanical properties of AISI 316LN stainless steel (parent metal) as a function of temperature, yield stress at zero plastic strain ($\boldsymbol{\sigma}_{y,0}$), kinematic hardening parameter (**C1**, **C2**), kinematic hardening parameter (γ_1, γ_2).

T [°C]	AISI 316LN				
	$\sigma_{y,0}$ [MPa]	C_1[MPa]	γ_1	C_2 [MPa]	γ_2
20	125.60	156435	1410.85	6134	47.19
275	97.60	100631	1410.85	5568	47.19
550	90.90	64341	1410.85	5227	47.19
750	71.40	56232	1410.85	4108	47.19
900	66.20	0.0500	1410.85	292	47.19
1000	31.82	0.0	1410.85	0.0	47.19
1100	19.73	0.0	1410.85	0.0	47.19
1400	2.10	0.0	1410.85	0.0	47.19

Table 7
Cyclic hardening properties of AISI 316LN stainless steel (parent metal) as a function of temperature, equivalent stress defining the size of the elastic range at zero plastic strain ($\boldsymbol{\sigma}_{|0}$), isotropic hardening parameter ($\mathbf{Q}_{inf}$), hardening parameter (**b**).

T [°C]	AISI 316LN		
	$\sigma_{|0}$ [MPa]	Q_{inf}	b
20	125.60	153.4	6.9
275	97.60	154.7	6.9
550	90.90	150.6	6.9
750	71.40	57.9	6.9
900	66.20	0.0	6.9
1000	31.82	0.0	6.9
1100	19.73	0.0	6.9
1400	2.10	0.0	6.9

where q is the power per unit volume, Q is total power deposited, (x,y,z) is the geometric centre of the distribution, and r_l, r_v, r_a are the radii of the distribution in the lateral, vertical and axial directions, see Fig. 1(b). The quantity V_a is not a user-specified parameter in FEAT-WMT, but is chosen automatically by the code on a particular mesh (and time-step in the case of a moving-torch simulations) so that the total power input to the work is Q (Smith et al., 2009b). Additionally, FEAT-WMT allows the heat source to be weaved in lateral (w_l) and vertical direction (w_v), where the weaving displacements are relative to the centre of gravity of the bead for the particular pass.

The source power-density distribution to be used to represent the heat source is then defined by the ellipsoid source parameters $(r_l, r_v, r_a, w_l, w_v)$ and power deposited by the 3D source which is calculated from I (welding current), V (arc voltage), torch speed v, and efficiency, η. Hence, the following (5) parameters were tuned in order to match the fusion zone (area, shape) and thermocouple responses: (i) the radii of the ellipsoid distribution in the lateral (r_l) vertical (r_v) and axial directions (r_a), (ii) the lateral (w_l) and vertical (w_v) weave paths, and (iii) the efficiency (η) which is initially set to 75% and then finely tuned to match the response of the far-field thermocouples (TC), e.g. TC5, TC7, TC8, TC9 and TC12 (see discussion below).

3.2. Mechanical modelling

The mechanical analysis employed mixed isotropic-kinematic hardening material properties. This is carried out in ABAQUS (ABAQUS, 2008) via a Lemaitre–Chaboche hardening model (Chaboche, 2008; Smith et al., 2009a), which allows the yield surface to either expand or contract and simultaneously translate. The Lemaitre–Chaboche model is primarily designed to predict the material response upon cyclic inelastic loading, where the cyclic load can be imposed either mechanically or thermally. The isotropic-kinematic formulation of this model allows simulation of both the Bauschinger effect and cyclic hardening with plastic shakedown which are both important phenomena during welding of austenitic stainless steels (Smith et al., 2009a).

(a) *The isotropic hardening component* defines the evolution of the radius of the yield surface, σ^0, as a function of the equivalent plastic strain. This is defined as follows:

$$\sigma^0 = \sigma_{|0} + Q_{inf}(1 - e^{-b\bar{\varepsilon}^{pl}}), \tag{2}$$

where $\sigma_{|0}$ is the yield stress at zero plastic strain and, $\bar{\varepsilon}^{pl}$ is equivalent plastic strain, Q_{inf} and b are material parameters. Q_{inf} defines the maximum change in the radius of the yield surface and b defines the rate at which the size of the yield surface changes as plastic strain develops (Smith et al., 2009a). The Q_{inf} and b parameters used in this study were derived from cyclic testing performed as part of the VORSAC 5th Framework EURATOM project (Keinänen, 1999).

(b) *The kinematic hardening component* is defined as a combination of a kinematic term and a relaxation term. It is modelled by the translation of the yield surface in the stress space, implemented mathematically by the evolution of the shift or back-stress tensor. Omitting any temperature or field variable dependencies, the kinematic hardening law is then defined as follows:

$$\dot{\alpha} = \sum_i \left[C_i \frac{1}{\sigma^0}(\sigma - \alpha)\dot{\bar{\varepsilon}}^{pl} - \gamma_i \alpha \dot{\bar{\varepsilon}}^{pl} \right], \tag{3}$$

where C_i and γ_i are material parameters, $\boldsymbol{\sigma}$ and $\boldsymbol{\alpha}$ are the stress and back-stress tensors, σ^0 is the equivalent stress defining the size of the yield surface, and $\dot{\bar{\varepsilon}}^{pl}$ is the equivalent plastic strain rate (Chaboche, 2008; Smith et al., 2009a). (Note that the back-stress tensor denotes the position of the centre of the yield surface in the stress space.) Two pairs C_1–γ_1, C_2–γ_2 and $\sigma_{|0}$ were fitted to monotonic tensile data up to 2% plastic strain, with γ_i constrained to be temperature independent.

In order to capture high temperature softening more realistically a two-stage annealing procedure was employed. This method defines "two isotropic annealing temperatures[1]": (i) a *lower annealing temperature*, **T1**, above which material ceases to exhibit any further isotropic hardening, but does not lose the hardening already accumulated at lower temperatures, and (ii) *an upper annealing tem-*

[1] The two isotropic annealing temperatures were chosen after review of cross-weld tensile data, in order to predict smooth variation of yield strength in the high-temperature heat affected zone adjacent to a weld bead.

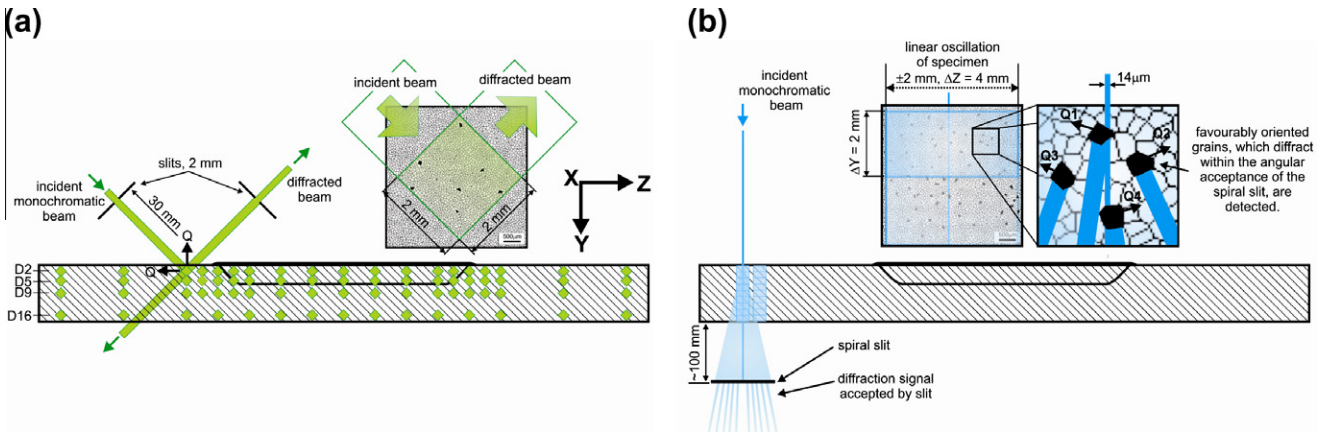

Fig. 4. (a) The schematic drawing of the neutron diffraction geometry, the positions of measuring points on the **D** plane (along the weld centerline, see Fig. 2(a)), and the gauge volume depicting a random number of grains satisfying the diffraction condition (black grains). (b) The schematic drawing of the synchrotron spiral-slit technique, and the gauge volume created by linear oscillation (Z direction) and diffraction data binning (*Y* direction). ΔY is set arbitrarily during the analysis of the data, not during the experiment, i.e. ΔY is "adjustable" and thus the *Y*-thickness of the light shaded box. All diffracting grains which are within the angular acceptance of the slit, are captured at once for each specimen *X*/*Z* position.

perature, **T2**, above which the equivalent plastic strain is set to zero, eliminating any prior isotropic hardening. In the current simulations $T1 = 800\ ^\circ C$ and $T2 = 1300\ ^\circ C$. Full details of this functionality and its ABAQUS implementation are given in ABAQUS (2007). The impact of high temperature softening on the kinematic hardening component is further handled by the kinematic hardening modulus C_1, C_2 which fall to zero at "kinematic annealing temperature[2]" 1000 °C (see Table 6). Note, that the back-stress tensor becomes zero, with the yield surface back at the origin, at the temperature where C_1, C_2 fall to zero, eliminating thus the kinematic hardening history. (see Section 7.1).

4. Diffraction measurements

4.1. Neutron diffraction technique

The neutron diffraction measurements were carried on the KOWARI diffractometer at the OPAL reactor at the Australian Nuclear Science and Technology Organisation, Lucas Heights, Australia. The diffraction geometry is schematically shown in Fig. 4(a). The vertically and horizontally focused neutron beam was produced by diffraction from the (004) planes of an elastically bent silicon crystal at a take-off angle of 90.4°. The resulting neutron wavelength was 1.53 Å. The $2 \times 2\ mm^2$ area of the incident beam was defined by a 2 mm wide and 2 mm high Cd slit, and placed 30 mm from the sample position in the incident beam. A second 2 mm and 10 mm high Cd slit was placed in the diffracted beam, 30 mm from the sample position, to produce a $2 \times 2 \times 2\ mm^3$ gauge volume over which the lattice spacing is averaged and which was centred on the sample rotation table. The size of the gauge volume was chosen to give adequate spatial resolution in the weld with high scattered intensity. The neutrons were recorded in a crossed-wire position sensitive detector with a vertical span of ±7.5°. Measurements were made with the {311} reflection of the face-centred cubic structure at a scattering angle of 92.8°. The {311} reflection was chosen because the "Type-2" (Hutchings et al., 2005) stresses are found to have the smallest numerical values for this reflection, at least for a uniaxial stress. Because of the grain size problem particularly in the weld region, the sample was rocked ±5° from its precise orientation.

Measurements were made: (i) along **D** lines which are on the **D** plane (Fig. 2(a)) running parallel to the weld bead at its centre at depths of 2 mm, 5 mm, 9 mm and 16 mm under the top plate surface (i.e. lines **D2**, **D5**, **D9**, **D16**), (ii) along **B** lines which are on the **B** plane (Fig. 2(a)) running perpendicular to the weld at the mid-length of the plate, at depths of 2 mm and 16 mm under the top plate surface (i.e. **B2**, **B16** lines), and finally (iii) along line **BD** which runs through the wall-thickness at the intersection of the **B** and **D** planes (Fig. 2(a)).

The lineshape in monochromatic diffraction is close to Gaussian and the peak positions were obtained by fitting a Gaussian upon a sloping background to the measured data. The fitting precision, $\Delta d/d$ was typically 2×10^{-5}, although, as described later, the accuracy is at least three times worse than this. The elastic lattice strain is simply calculated from the relative shift of the d-spacing with respect to the stress-free d_0-spacing, as:

$$\varepsilon_{ij}^{311} = (d^{311} - d_0^{311})/d_0^{311}, \tag{4}$$

where d_0^{311} is a suitable stress-free reference spacing measured in reference specimens cut as small cuboids (see Section 2) from the parent and weld metal (see Fig. 3(a)). Macroscopic stress components, σ_{ij}, where the numerical superscripts refer to directions in the sample, are related to the elastic strains in analogy with Hooke's Law by

$$\sigma_{ij} = \frac{E^{311}}{(1+\nu^{311})}\left[\varepsilon_{ij} + \delta_{ij}\frac{\nu^{311}}{(1-2\nu^{311})}\varepsilon_{kk}^{311}\right], \tag{5}$$

where E^{311} and ν^{311} are known "diffraction elastic constants" (DEC) relating strain in the {311} lattice planes to the macroscopic stress. They may be either measured or calculated with a good accuracy based on the self-consistent Eshelby–Kröner model (Kröner, 1958) and using single crystal elastic constants for austenitic stainless steel 316L. The values used here were $E^{311} = 183.6$ GPa and $\nu^{311} = 0.306$.

4.2. Synchrotron diffraction technique

The diffraction experiments were conducted at the beamline ID15A at the European Synchrotron Radiation Facility (ESRF) in

[2] The "kinematic annealing temperature" is the temperature at which the material may be considered to be perfectly plastic with no work hardening, so the back-stress is always zero. This temperature may be deduced from high temperature tensile tests. Data were available for temperatures up to 1100 °C, and 1000 °C was chosen as a convenient bounding temperature.

Grenoble, France. Monochromatic high-energy synchrotron radiation with a wavelength of 0.0114 nm was focussed with Compound Refractive Lenses (CRLs) to a beamsize of 14 μm × 14 μm. The weld specimen, carrying the identification mark "3-1A", was investigated in transmission geometry with the incoming beam parallel to the *Y*-axis (Fig. 4(b)). The batch of d_0 reference specimens with the identification mark *Z* was produced in an identical way as the d_0 reference specimens used for neutron diffraction (see Section 2). The spiral slit technique (Martins and Honkimäki, 2003) was used to obtain a depth and phase resolved diffraction signal. To enhance the measurement statistics the specimen was linearly oscillated parallel to the *Z*-direction in a range of $\Delta Z = 4$ mm as is schematically shown in Fig. 4(b). In addition, at each nominal specimen *X*/*Z*-position at least two images were recorded with an offset of $\Delta X = 0.5$ mm between each image. In order to obtain a full 3D map of the residual stress field associated with the weld, the measurement pattern in the *X*/*Y*-plane was divided into three grid scans and four lines. One grid covered the entire specimen with a 10 mm × 10 mm mesh, and two grids with a mesh of 2.5 mm × 2.5 mm provided a more detailed view of the weld start and stop areas (Martins et al., 2010). The complete data set consists of over 2200 images allowing proper 3D mapping.

Because of the coarse grain structure and the resulting spotty diffraction patterns a novel data analysis procedure was applied to determine the in-plane macrostrain components. Rather than performing a powder-like analysis with the fitting of diffraction peaks a procedure based on the centre of mass position of diffraction spots from individual grains was applied (Martins et al., 2010). The diffraction geometry in conjunction with the spiral slit geometry allowed then to determine the nominal *X*/*Y*/*Z*-position of each detected spot. To obtain the values for the in-plane strain components ε_{11}, ε_{33}, and ε_{13}, an over-determined system of linear equations was solved, involving the unknown strain tensor components, specimen and scattering vector depending variables and the deviation, with respect to the d_0 reference, of the scattering angles of grains of the specific gauge volumes of interest (see Martins et al., 2010 for details). The diffraction spots from the austenite planes {111}, {200}, {220}, {311}, and {222} were used in the stress analysis. Residual stresses were then calculated based on a *biaxial stress state assumption* (assuming the normal σ_{22} stress component being zero, $\sigma_{22} = 0$) and using diffraction elastic constants (DEC) weighted by the distribution of the diffraction spots over the different {hkl} at each individual gauge volume position. As in the neutron diffraction data analysis, the DEC were calculated based on the self-consistent Eshelby–Kröner model (Kröner, 1958) and using the same single crystal elastic constants.

5. Modelling results

5.1. Thermal modelling

The moving heat source thermal solution was found using all known heat source parameters (e.g. arc voltage, travel speed, etc. see Table 2) and optimized unknown heat source parameters, i.e.: (i) η (efficiency), (ii) r_l, r_v, r_a (lateral, vertical and axial radii of Gaussian heat source, Fig. 1(b)), and (iii) w_l, w_v (lateral and vertical weave of heat source) see Section 3.1. The welding efficiency (η), the only unknown *global* welding parameter, was optimized by matching the measured temperatures at far-field mid-length thermocouples. Note, that the far-field thermal solution is unlikely to be affected by the change in fusion boundary profile (Smith and Smith, 2009b). The far-field thermocouples are those far enough from the weld torch, hence the heat source can be approximated as a point source, with no significant impact of the heat source size and shape on the modelling result. The far-field thermocouples are considered to be those on the back-face of the specimen (TC7, TC8, and TC9) and those on the top-surface further from the weld centreline, i.e. TC4, TC5, TC6 and TC12 (see Fig. 4). The mid-length thermocouples, are those which are close to mid-length of the sample so that they respond to steady-state conditions i.e. TC2, TC5, and TC7-TC12. Hence, during the optimization process the main priority was focused on the responses of the following six far-field mid-length thermocouples: TC5, TC7, TC8, TC12, and TC9 which are suitably positioned for the weld efficiency calibration. (Note, that the TC10 is very close to the weld hence it is likely to be affected by the arc shine and is thus considered not to be suitable for the heat-source optimisation process. Nevertheless, the response of this thermocouple is still reasonably well captured.) The remaining *local* heat source parameters, the lateral, vertical, and axial radii (r_l, r_v, r_a), as well as the extent of lateral and vertical weaving (w_l, w_v) were optimized by matching the measured mid-length fusion boundaries (size and shape) as revealed by transverse macrographs in Fig. 6.

5.1.1. Thermocouple responses and welding efficiency optimization

The thermocouple responses for two instrumented weld specimens marked "2-1A" and "3-1B" are shown in Fig. 5. Note that some thermocouples are located at the same distance on both sides from the weld centreline, e.g. TC5 and TC12 (±18 mm from centerline), these are shown together in the present plots. It is clear from Fig. 5, that the spread in measured peak temperatures varies between 20 °C to 80 °C in the case of near-field thermocouples as well as those at the start–end and stop-end of the bead (TC1, TC3). In the case of the far-field thermocouples the spread is considerably narrower. This helps to optimize the heat source efficiency correctly. The scatter in the measured thermocouple responses for near field thermocouples can stem from different sources (Smith and Smith, 2009b) e.g. the poor thermal contact, positioning errors, weld bead length or position variation between specimens, and the impact of arc shine on top surface thermocouples. Top surface near-field thermocouples are more likely to be sensitive to the arc shine, as well as positioning errors.

Let us now compare the predicted and measured temperatures in Fig. 5. By inspecting the top-surface near-field thermocouples TC1, TC2, TC3, TC11 results it becomes apparent that the predictions are somewhat on the lower side of the measurements for the 2nd and 3rd passes. The differences between measured and predicted temperatures are more pronounced at the start–end and stop-end locations (TC1, TC3). This effect is most probably due to slightly varying stop and start positions (decided by the welder, see Section 2) and the complexity of the three-dimensional heat conduction in these start and stop-ends of the weld bead. A further consideration is the effect of arc shine on the near-field thermocouples which would be greatest for the 2nd and 3rd passes while the 1st pass is partially hidden from thermocouples. As further seen from Fig. 5, the response prediction of the top-surface far-field thermocouples TC4, TC5, TC6, TC12 is noticeably better. Most importantly, the back-face far-field thermocouples (TC7, TC8, TC9) which were preferentially used for optimization of the heat source efficiency are predicted with an excellent accuracy (±5 °C). This optimization process for all three passes has led to the efficiencies close to 75% (see Table 2) which is a typical efficiency for the tungsten-inert-has (TIG) welding process (Smith and Smith, 2009a,b). As one would expect the efficiency slightly falls from PASS.1 which is inside the slot itself to PASS.3 which is at the top-surface, where there exists a higher opportunity for heat losses.

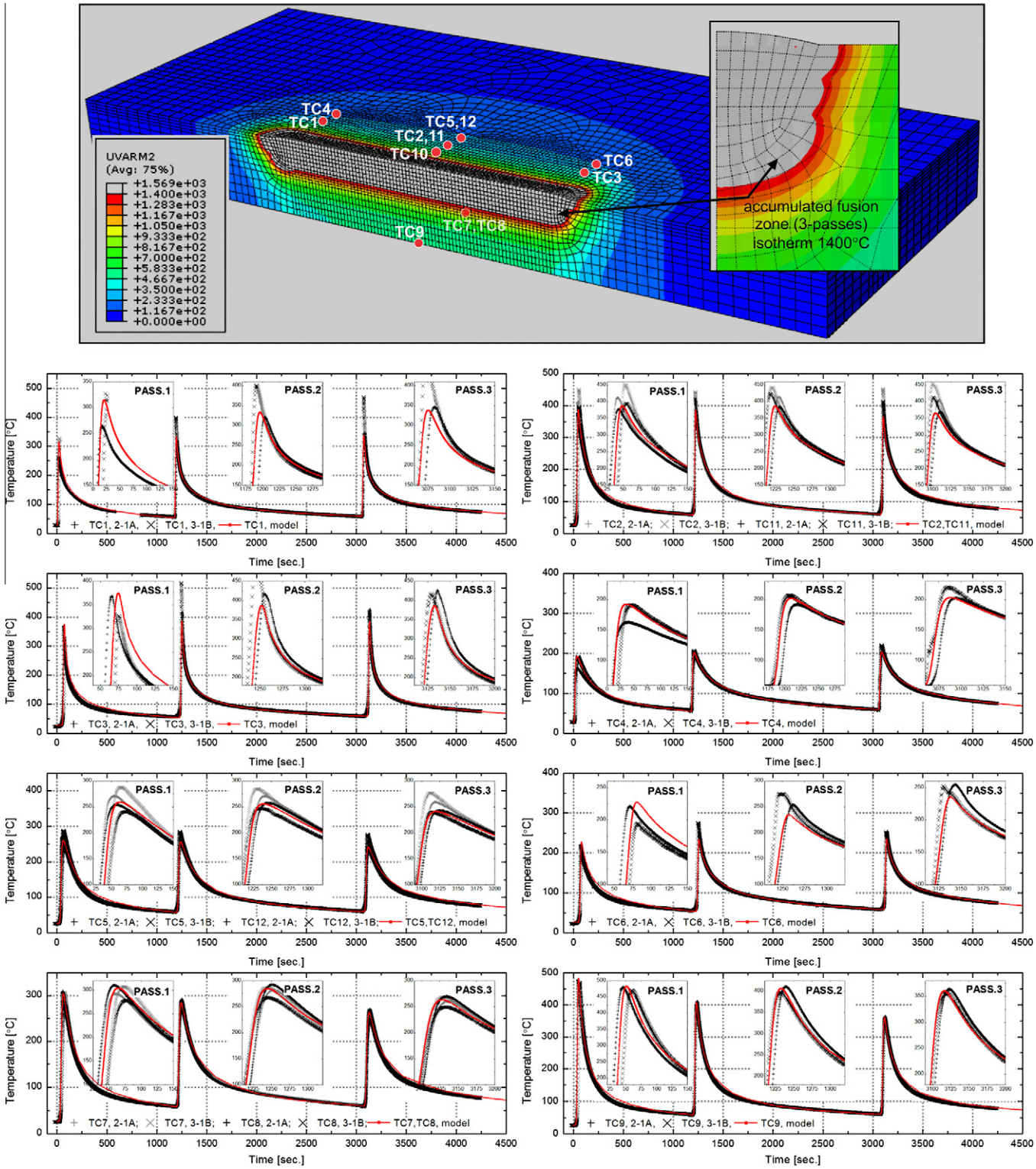

Fig. 5. (Top) Accumulated fusion zone (grey region-1400 °C isotherm) and position of the thermocouples shown on the Abaqus half model. (Bottom) Measured response of all thermocouples (symbols) compared with the finite element predictions.

5.1.2. Weld fusion zone and shape/size heat source optimization

Fig. 6 shows the mid-length section micrographs for all three passes with the prediction of the fusion zone in FEAT-WMT .(Smith, 2009) on the left and in ABAQUS (ABAQUS, 2008) on the right. The predicted fusion zone is presented as a temperature contour plot showing the 1400 °C isotherm. The 1400 °C isotherm closely corresponds to the melting point and thus to the weld fusion boundary. It is, therefore, readily compared with obtained micrographs (Smith and Smith, 2009b; Truman and Smith, 2009).

In order to match the observed fusion zone from the mid-length weld section weaving of the heat source had to be incorporated into the simulations even though the actual welding process was

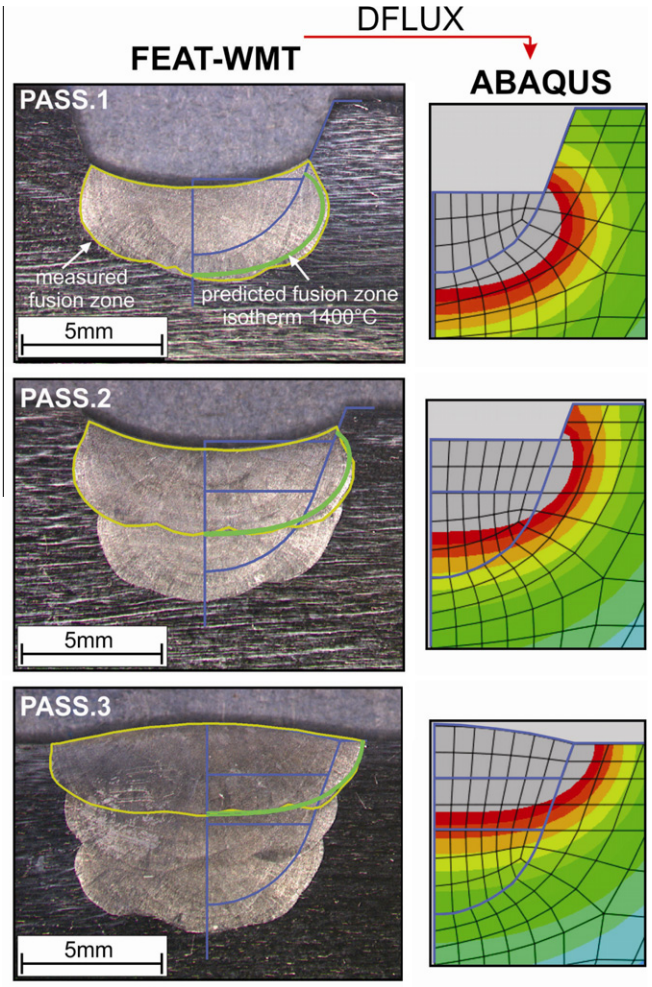

Fig. 6. Comparison of the observed fusion zone in the plate mid-length (steady-state region) and the predicted fusion zone (grey region-1400 °C isotherm).

performed without weaving. It has been, however, observed that a combination of pulsed welding and the introduction of filler wire into the centre of the weld pool produces a weaving-like effect. Note that the filler wire tends to chill the weld pool centre, which leads to a broad weld bead. To simulate this effect in addition to the optimization of the size of the Gaussian heat source defined by the lateral, vertical and axial radii (r_l,r_v,r_a), it needed to be laterally and vertically weaved (w_l,w_v). The same can be also achieved by either elongating the heat source in the transverse plane, or by weaving a near-spherical heat source. Both these options result in the correct fusion boundary profile: the weaved source was chosen for convenience.

Fig. 6 makes a direct comparison between the predicted and measured bead profiles. It can be seen that an almost perfect match (size-wise as well as shape-wise) was achieved between the measured and predicted fusion zones for individual passes. 101%, 100%, and 100% of the measured fusion area was achieved in the simulations for passes 1, 2 and 3, respectively. The overall cumulative fusion zone of all three passes is shown in Fig. 5 (top) and all optimized heat source parameters (*global*, *local*) are tabulated in Table 3. These results provide confidence in the obtained thermal solution which is used as an input into the following mechanical analysis in order to predict the residual stress field associated with the weld. Note, that the global heat input is the most important thermal variable affecting the mechanical predictions (Smith and Smith, 2009b).

5.2. Mechanical modelling

Typical ABAQUS 3D contour plots of longitudinal (σ_{33}) and transverse (σ_{11}) stresses, viewed from the top of the plate, with a cross-section along the centre of the weld bead and with a transverse cross-section at the mid-length are shown in Fig. 7 (top) and Fig. 8 (top), respectively. In Fig. 9(a) and (b) (left) are shown predicted residual stresses in all three principal directions on the longitudinal weld bead centre-line, plane **D**, and on a transverse cross-section at mid-length, plane **B**, respectively. It is clear from present contour plots that the high tensile transverse (σ_{11}) stresses are predicted beneath the weld bead peaking under the weld stop-end, and also on the top surface on the plate alongside the weld bead, again peaking at the weld stop-end. These transverse (σ_{11}) tensile stresses in the proximity of the weld are balanced by the compressive stress field extending from the start–end and stop-end of the weld to the transverse edges of the weld plate. High tensile longitudinal (σ_{33}) stresses are predicted beneath the slot in the heat affected zone (HAZ) and in the material applied during the first and second pass. Residual stresses in the last weld pass are tensile but roughly 50 MPa lower than those predicted in depth in the range from 2 to 9 mm under the top surface. It is further clear that there are higher tensile longitudinal (σ_{33}) stresses predicted on the back face beneath the weld bead. From the contour map on the transverse cross-section can be seen that the high longitudinal (σ_{33}) residual stress field is around the whole weld area. These tensile longitudinal (σ_{33}) stresses associated with the weld area are balanced by compressive stress field far from the weld bead spreading towards the longitudinal plate edge.

5.2.1. Predicted residual stresses along D lines

Lines **D2**, **D5**, **D9**, and **D16** run parallel to the weld bead on the symmetry plane at the centre of the weld bead, 2 mm, 5 mm, 9 mm and 16 mm under the top plate surface respectively. Namely, line **D2** runs at the interface between the elements of the second pass (PASS.2) and the third pass (PASS3), line **D5** runs through the elements of the first pass (PASS.1) close to the bottom of the slot, line **D9** runs at mid-thickness of the plate, about 2 mm under the fusion zone of the first welding pass and at the edge of the 800 °C isotherm and finally line **D16** runs 2 mm under the back face of the sample.

Residual strains and stresses in all three principal direction along all **D** lines predicted in both performed simulations are shown in Fig. 7. It is clear from the present results that in general the residual stresses have very similar trend along lines **D2**, **D5** and **D9**. As seen from Fig. 7, the transverse (σ_{11}) stress is predicted to be always compressive at either of the transverse edges and rise sharply into tension at the interface between the weld metal and parent plate. In the weld itself (lines **D2, D5**) the transverse (σ_{11}) stresses gradually increase from the start–end of the weld towards the stop-end of the weld, peaking at the weld-parent metal interface. This is a real effect caused by the moving heat source. It cannot be captured by simple "block-dumped" analyses which deposit the whole bead length at once (see Muránsky et al., 2010). The effect of the moving heat source is much less pronounced along line **D9**. As one would expect based on the sample geometry the normal (σ_{22}) stress along these three lines are roughly zero and seems to be more-or-less symmetric around the mid-length of the specimen. There is a "zigzag" at the interface between the parent metal and weld metal which undergoes full annealing above 1300 °C. These clearly visible discontinuities at the weld-parent metal interfaces are caused by the ABAQUS data extraction across the annealing boundary. The longitudinal (σ_{33}) stresses are predicted to be zero at both transverse edges and similarly to the transverse (σ_{11}) stresses they rise sharply at the start–end of the weld and

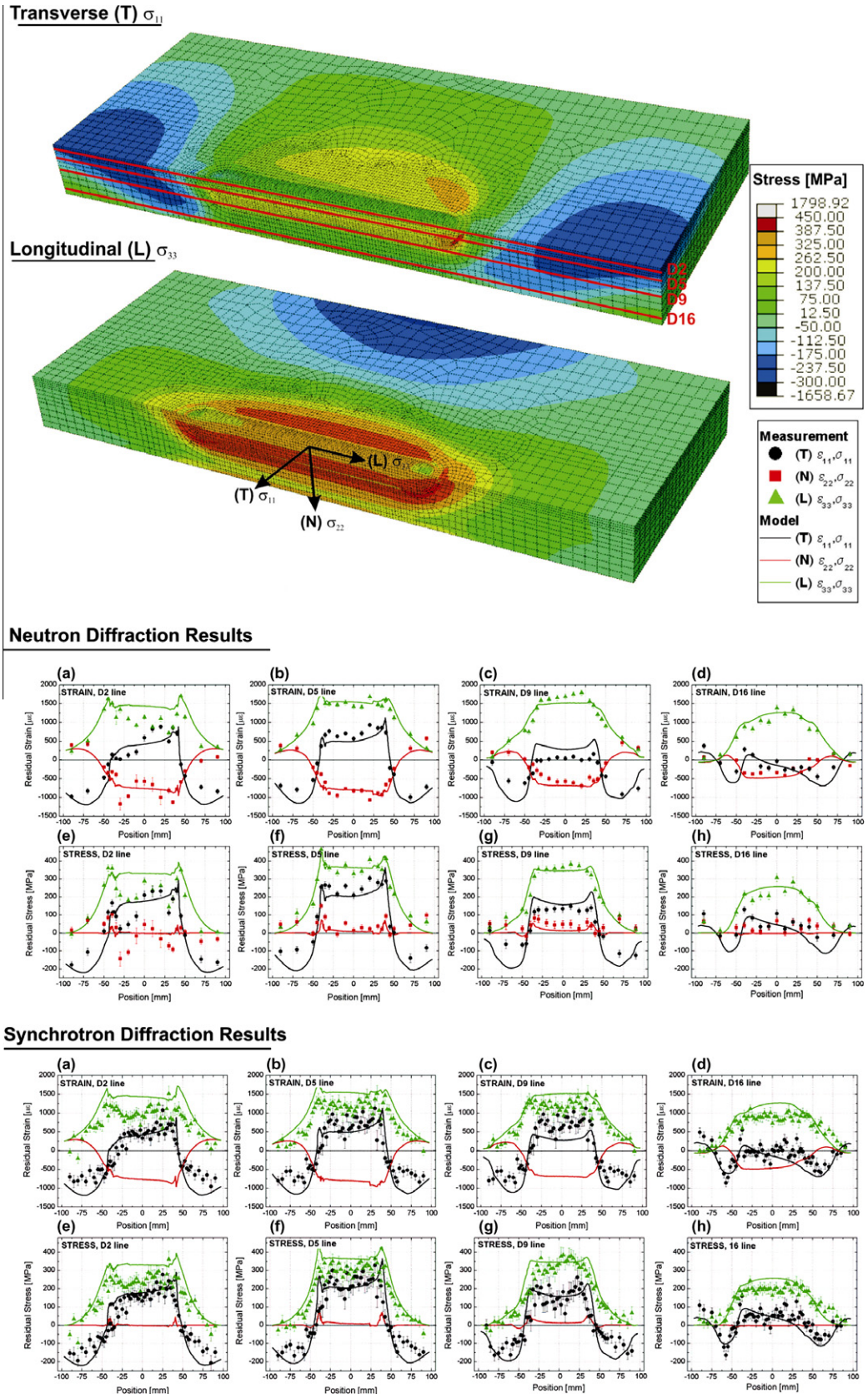

Fig. 7. (**top**) 3D contour plots of predicted transverse (σ_{11}) and longitudinal (σ_{33}) residual stresses. (a)–(d) Predicted elastic residual strains along the **D** lines compared with the neutron diffraction-measured and synchrotron-measured data. (e)–(h) The predicted residual stresses along the **D** lines compared with the experimentally obtained (i.e. recalculated from the measured elastic residual strains) residual stresses.

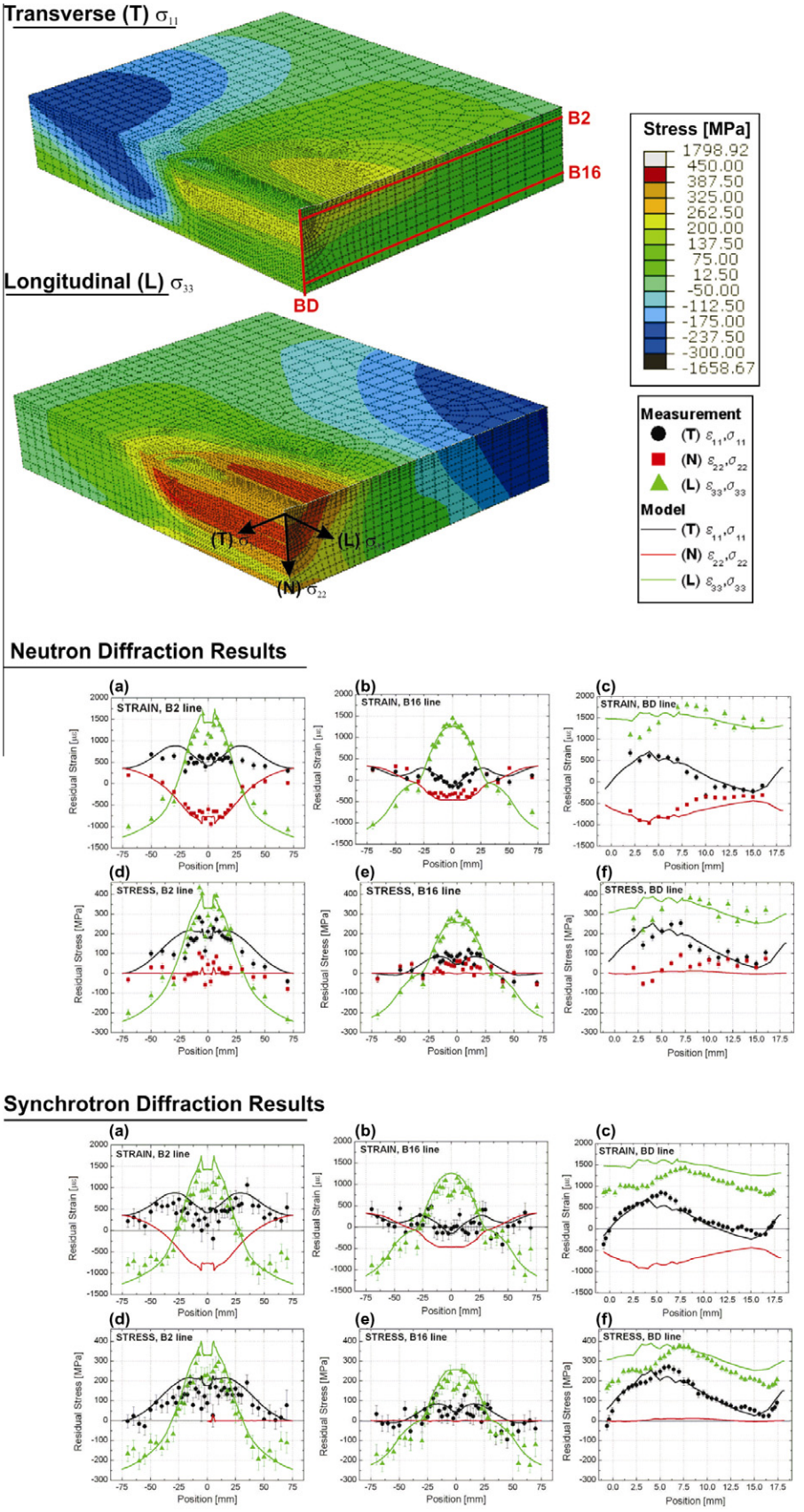

Fig. 8. (Top) 3D contour plots of predicted transverse (σ_{11}) and longitudinal (σ_{33}) residual stresses. (a)–(d) The predicted elastic residual strains along the **B** lines and **BD** line compared with the neutron diffraction-measured and synchrotron-measured data. (e)–(h) The predicted residual stresses along the **B** lines and **BD** line compared with the experimentally obtained (i.e. recalculated from the measured elastic residual strains) residual stresses.

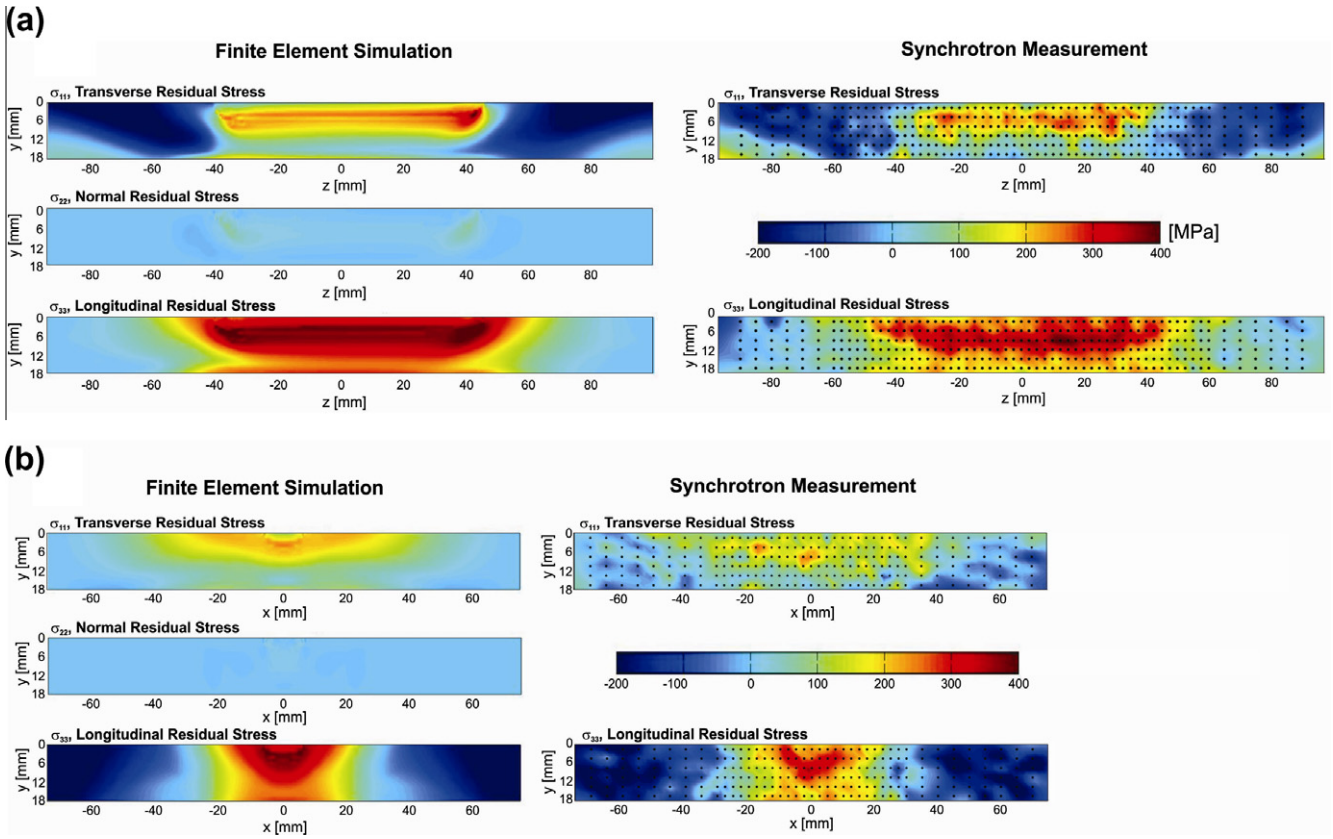

Fig. 9. Comparison of the predicted and synchrotron-measured transverse (σ_{11}), normal (σ_{22}) and longitudinal (σ_{33}) residual stresses on the (a) **D** plane and (b) **B** plane.

falls at the stop-end of the weld. They are being fairly constant in tension the along the weld itself, even though there are sharp peaks at the weld-parent metal interfaces at the start–end and stop-end positions. It is further clear that the moving heat source does not have the same effect on the longitudinal (σ_{33}) stress as was observed for transverse (σ_{11}) stress.

The residual stress profile along line **D16** on the back face is different from the other **D** lines discussed above. As one would expect the transverse (σ_{11}) and longitudinal (σ_{33}) stresses are in general lower in magnitude and the stress profile is different, particularly for the transverse (σ_{11}) stress. It is interesting to see that transverse (σ_{11}) stress is tensile under the start–end and compressive under the stop-end of the weld bead. The longitudinal (σ_{33}) stress is zero at the transverse edges and roughly constant underneath the weld. The normal stress (σ_{22}) is clearly zero along line **D16**.

5.2.2. Predicted residual stresses along B lines

Lines **B2** and **B16** are running perpendicular to the weld at the mid-length of the plate, 2 mm and 16 mm under the top plate surface. Namely, line **B2** crosses the weld metal only in the plate centre (±6 mm slot ±1 mm fusion zone), and line **B16** runs close to the back face fully in the parent metal.

Residual strains and stresses in all three principal directions along both **B** lines predicted are shown in Fig. 8. Note, that the results were reflected along the symmetry plane (Fig. 2(b)) for easier comparison with the measurements. It is clear from the present results that the stress profiles in along both **B** lines are very similar differing only in the magnitude. As one would expect the stresses along line **B16** are lower comparing to line **B2**. The transverse (σ_{11}) stresses are zero at the both longitudinal edges and gradually increasing towards the weld peaking at the weld-parent metal interface. The longitudinal (σ_{33}) stress also peaks at the weld-parent metal interface, but it is negative at the longitudinal edges.

5.2.3. Predicted residual stresses along BD line

Line **BD** runs through the wall-thickness at the mid-length of the plate on the symmetry plane (Fig. 2(b)). This line crosses the weld-parent metal boundary and a number of important isotherms: (i) the 1400 °C isotherm defining the fusion boundary zone, (ii) the 1300 °C isotherm defining the *upper annealing temperature* (**T2**) above which material loses all accumulated plastic strain, and (iii) the 800 °C isotherm defining the *lower annealing temperature* (**T1**) above which material ceases to exhibit any hardening, though it does not lose already accumulated plastic strain (see Section 3.2). From the present results in Fig. 8 can be seen that the transverse (σ_{11}) and longitudinal (σ_{33}) stresses are not only always positive but also have a similar profile through the wall-thickness. They are reaching a maximum ~7 mm in depth (at the weld-parent interface, i.e. fusion zone edge), then gradually fall down reaching a minimum at approximately 15 mm in depth and then rise again towards the plate back face. The normal (σ_{22}) stress is again very close to zero as one would expect for the given sample geometry.

6. Measurement results

6.1. Neutron diffraction results

Neutron diffraction results in the three principal directions measured along the lines required by the measuring protocol .(i.e. **B2**, **B16**, **D2**, **D5**, **D9**, **D16** and **BD**) are shown together with the finite-element simulations in Figs. 7 and 8. The error in the experimental strain varies between 50 με in the parent to 80 με

in the weld. This gives an average error on calculated stress of about 25 MPa. It is, however, necessary to emphasize that this error calculation is based on the peak-fitting error only and does not include any error produced by the grain statistic problems.

In an ideal experiment where the grain size is about 20 μm, there are hundreds of grains contributing to the diffraction pattern and these are distributed evenly within the gauge volume. Based on the statistical analysis of the measured and ideal diffraction intensity, in the present situation there were of the order of ten or less grains contributing to the diffraction pattern, particularly in the weld metal. The fluctuations in intensity at the top of the weld were more marked than at the bottom of the weld and parent metal corresponding to fewer grains in the gauge volume and hence larger grain size (see record from the array detector in Fig. 3). This leads to two contributions to the systematic error. Firstly there is low sampling of the distribution of strains exhibited by the grains and secondly, the few illuminated grains may be offset from the centre of the gauge volume in the horizontal plane and therefore give rise to systematic errors in the peak position. In order to minimize this kind of error contribution, the sample was rocked over an angular range of ±5° about an axis perpendicular to the scattering plane and centred on the gauge volume. Nevertheless, the fluctuations in the peak intensity (reflecting number of grains in which are favourably orient in the gauge volume) mainly in the weld led to scattering of the recalculated residual strains/stresses (see results along **D2** line in Fig. 7(e)). This kind of uncertainty is hard to include in the calculation, but the real error can be three-times as large as the fitting-based error, mainly in the area with large/larger grains (i.e. weld metal).

In the d_0 measurements, it was established that there was no difference, outside the standard deviation, between longitudinal, transverse and normal direction so that intergranular strains are negligible for the {311} reflection. Additionally, the lattice spacing at the bottom of the weld is the same (within the standard deviation) as the parent, but different from the top of the weld (this in contrast with synchrotron data, see below). The

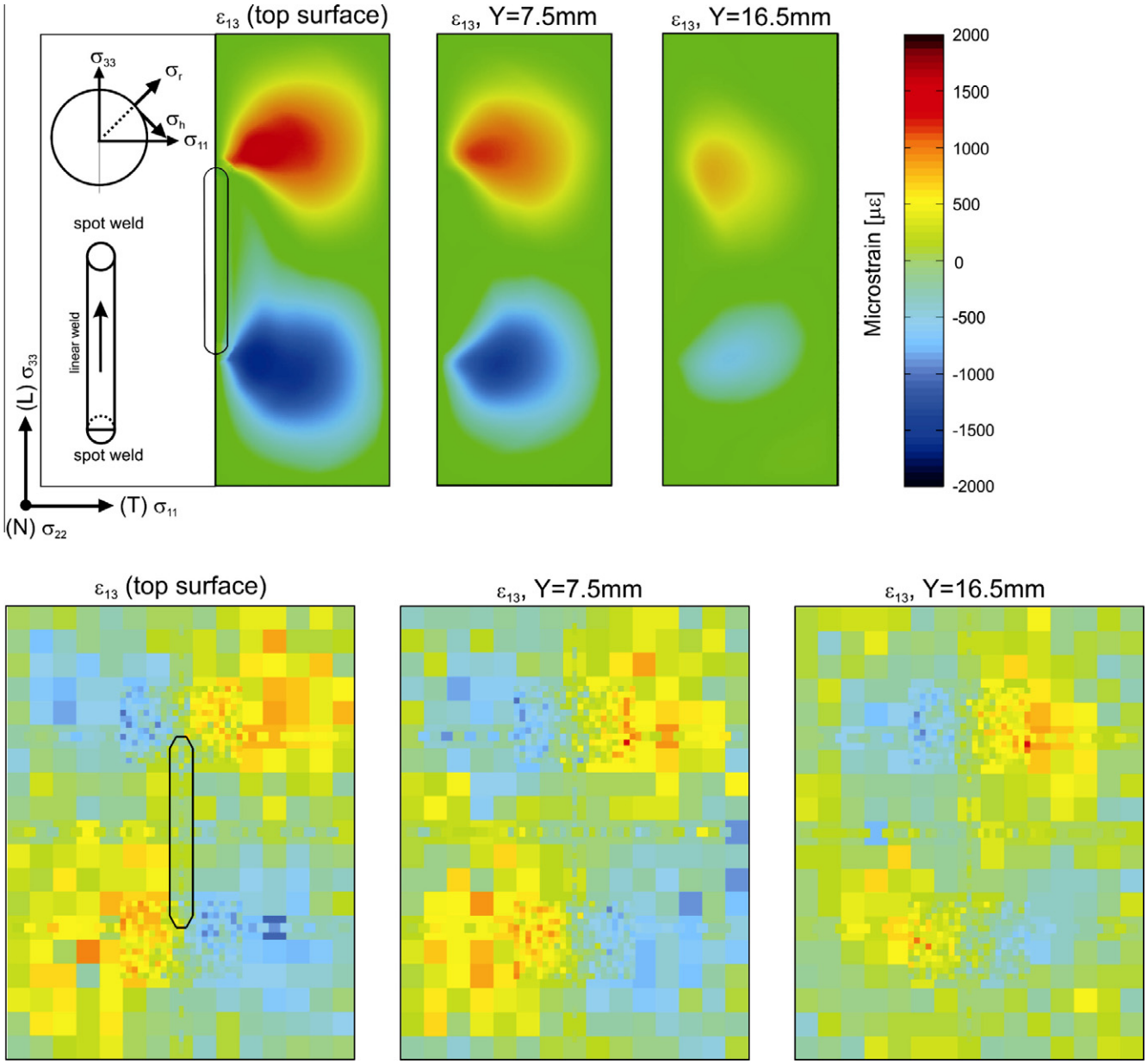

Fig. 10. Comparison of the predicted (**top**) and synchrotron-measured (**bottom**) shear (ε_{13}) residual strain at different Y position (through the plate thickness), Y = 0 mm (top surface), Y = 7.5 mm, and Y = 16.5 mm. The calculated shear strain is shown for the right hand side of the plate looking from above.

reference lattice parameter for the parent was used to derive strains from the measured lattice spacings for all the measurements except those at 2 mm below the top surface of the plate in the weld. Neutron diffraction results are compared and discussed later together with the synchrotron results and finite-element simulations.

6.2. Synchrotron diffraction results

Synchrotron diffraction results along the requested lines (i.e. **B2**, **B16**, **D2**, **D5**, **D9**, **D16** and **BD**) together with the simulations are shown in Figs. 7 and 8. Note that only the in-plane residual strains were measured (normal through-wall thickness stresses (σ_{22}) are assumed to being zero). Figs. 9 and 10 show the experimental residual stress maps of two measured stress components and in-plane shear strain component (ε_{13}), respectively. Note that the pixel size in the experimental maps in Fig. 10 changes according to the mesh and scan density.

The errors are in the range of 120–190 $\mu\varepsilon$, that leads to an average error on calculated stresses of 40 MPa. Unlike the fitting error in the neutron experiment this error is closer to the real measuring error. This is due to the fact that each diffraction spot in the synchrotron pattern comes from one grain only due to the very small gauge volume. Hence, the grain is more likely to be in the middle of the gauge volume which reduces the contribution to the systematic error. In the synchrotron data analysis the actual spot position is used as a center to reflect the lattice parameter whereas in the neutron diffraction data analysis the nominal center of the gauge volume is used even though the Bragg image of the crystalline is not centered (and it is not know where in the gauge volume it is).

As opposed to the neutron diffraction measurements, the synchrotron diffraction measurements showed an increase of the d_0 reference lattice parameter from the weld top to the weld bottom and to the parent material (Martins et al., 2010). There appear to be two main reasons why the d_0 measurements by synchrotron X-ray diffraction show a small difference between parent material and weld-bottom material. Firstly, the measurements were done on a different batch of d_0 specimens, this however should not play a role considering that all d_0 samples where extracted from the same specimen. Secondly, the neutron diffraction measurements were averaging over a larger gauge volume, smoothing local variations within the d_0 specimens. A detailed description and discussion of the synchrotron results, with the exception of the shear strain map (Fig. 10, discussed below), can be found in Martins et al. (2010).

7. Discussion and model validation

7.1. Material response during welding process

Before discussing the comparison of predicted and measured residual stresses it is important to understand that the residual stress state of the material depends on the thermo-mechanical history experienced by the material during the welding process. Since the material response depends on the temperature which it is experiencing, the residual stresses stemming from the misfit between the plastically deformed region and the remaining unaffected region (Hutchings et al., 2005) inevitably vary with distance from the heat source. In the other words, if the spatial gradient in temperature is not sufficient to cause plastic deformation, then there would be no residual stresses after welding (Hutchings et al., 2005). Fig. 11 shows the predicted development of stresses (material response) as well as development of the back-stresses (i.e. shift of the centre of the yield surface) in three principal directions in six different nodes across the plate thickness in the plate mid-length. Node N1 is in the first deposited weld bead, and the remaining nodes are in parent material at increasing distances from the weld. Fig. 11 shows the development of the transverse (σ_{11}), normal (σ_{22}), longitudinal (σ_{33}) stresses (straight lines), the direct back-stress ($\alpha_{11}, \alpha_{22}, \alpha_{33}$) components (dashed lines) and equivalent plastic strain (PEEQ), and the temperature, as a function of time. PASS.1 is plotted in the left hand column, PASS.2 in the centre column, and PASS.3 in the right hand column. Note that the back-stress components change when active plastic flow is taking place, and record the shift of the centre of the yield surface. They record the development of kinematic hardening, and the extent of the Bauschinger effect. PEEQ is a scalar representing accumulated plastic strain in all directions, and determines the radius of the yield surface, or the amount of isotropic hardening.

Consider first PASS.1, plotted in the left hand column. The response of the weld bead, node N1, is straightforward monotonic loading: as the molten bead cools down it develops tensile stresses, highest in the longitudinal direction (green), with tensile back-stress components and about 1.5% accumulated plastic strain. Parent material beneath the bead is always loaded first in compression during the heating phase of the transient, with the majority of the plastic strain accumulated during heating, and then goes into tension during the cool down phase of the transient. The precise response depends upon the peak temperature achieved. Thus at node N2, the peak temperature exceeds 1300 °C, so even though the material yields extensively in compression during heating, both the equivalent plastic strain and the back-stress are eliminated when material reaches 1300 °C. A relatively small amount of plastic strain accumulates in tension during cooling, while the back-stress components are fairly strongly tensile because of the loss of the kinematic hardening memory at high temperature. In contrast, at Node N3, the peak temperature is about 1100 °C, so the approx. 8% plastic strain that accumulates in compression during heating is retained, with a further 1% accumulating in tension during cool down. The compressive back-stress is eliminated at the end of the heating phase since the temperature exceeds 1000 °C, and rises to a similar level to N2 during cooling. The stresses at N3 at the end of PASS.1 are higher than those at N2, due to the increased level of retained isotropic hardening. Node N4 only reaches 900 °C, so both the kinematic and isotropic hardening components accumulated during heating are retained. The back-stress components at the end of cool down are close to zero because the compressive shift of the yield surface during heating has not been eliminated, and the final longitudinal and transverse direct stresses are approximately 100 MPa lower than at N3, due almost wholly to the reduced back-stress. Behaviour near the back face at N5 and N6 is more complex. These regions accumulate equivalent plastic strain and compressive back-stress only during the heating phase of the transient, and the compressive stresses developed during the heating phase do not reverse, suggesting that this region is not on the yield surface at the end of PASS.1.

Now consider PASS.2, plotted in the centre column. In general, the stress field present at the end of PASS.1 is almost wholly eliminated by compressive plastic flow during the heating phase of the transient, and the subsequent response at each node is similar to that observed during PASS.1 at deeper nodes that achieved the same temperature in PASS.1. Thus N1 behaves in the same fashion as did N2 during PASS.1, and N2 behaves like N4. Near the back face, where the peak temperatures are much lower, the responses during PASS.2 are qualitatively very similar to those during PASS.1. Broadly speaking, the same behaviour is observed in PASS.3 (see discussion below).

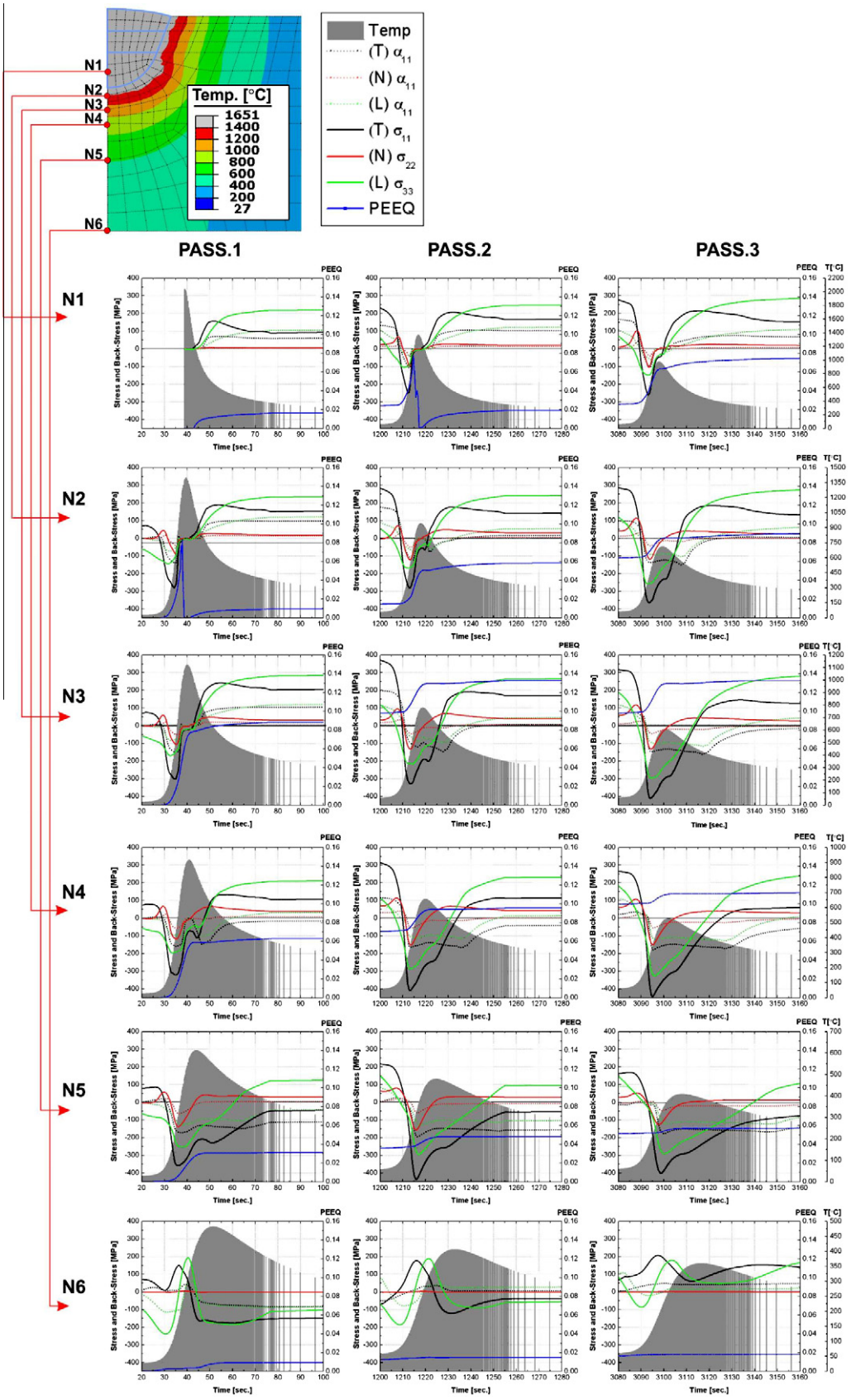

Fig. 11. Development of the residual stresses (σ_{11}, σ_{22}, σ_{33} – straight line), back-stresses ($\alpha_{11}, \alpha_{22}, \alpha_{33}$), and equivalent plastic strain (PEEQ) at different position across the weld thickness in the sample mid-length on the B plane as a function of time. The location of nodes in *Y* direction is as follows: N1 ~ 5 mm, N2 ~ 7 mm, N3 ~ 7.8 mm, N4 ~ 9 mm, N5 ~ 12 mm, N6 ~ 18 mm. or Fig. 11 depends on the reviewer's opinion,... the authors still prefer the original above figure with all the back-stresses for the completeness, because removing the transverse and normal back-stresses does not really clear the picture that much,... really just matter of opinion,....

What do these results mean? It is clear that the final stress field is most influenced by PASS.3, since each successive pass generates enough plastic flow to wash out the stress field existing at the end of the previous pass. It is also clear that most plastic flow is developed in compression during heating. It is thus very important that the material hardening model contains a kinematic component, otherwise the Bauschinger effect will not be captured.

Beyond this, the results show that appropriate handling of high temperature softening effects is also very important. The effect depends on the hardening component being considered. Thus, the heating phase generates compressive back-stresses. If no "kinematic annealing" occurs, these will be retained into the cooling phase, will displace the yield surface into compression, and reduce the magnitude of the tensile residual stresses present at the end of welding. If the back-stress is eliminated, then the yield surface returns to the origin at the end of heating, and displaces into tension during cooling, increasing the magnitude of the final tensile residual stress field. This may seem counter-intuitive ("annealing" increases stresses), but is a consequence of the elimination of the Baushinger effect by annealing. In contrast, elimination of prior isotropic hardening has the expected effect of reducing the level of the final tensile residual stresses, since the yield surface then has a smaller radius.

7.2. Comparison of predicted residual stresses with measurements

In order to validate the modelling results the predicted residual stresses are compared with neutron diffraction and synchrotron diffraction residual stress measurements. First let us compare the overall stress field by comparing the predicted and synchrotron-measured stress maps on the **D** and **B** planes in Fig. 10. It becomes clear from the present results that the overall prediction of the stress field is in a very good agreement with the experimental synchrotron results. The high tensile transverse (σ_{11}) stress on the **D** plane is predicted in the weld region, whereas the high tensile longitudinal (σ_{33}) stress seems to be more-or-less across the plate thickness spreading out of the weld region. This is in a reasonably good agreement with the synchrotron results, even though the measurements are somewhat spottier but this is not unusual for experimentally measured data. The stress field in the plate mid-length on the **B** plane is also reasonably well captured particularly for the longitudinal (σ_{33}) stress component. Most importantly, the modelling results clearly show that the normal (σ_{22}) stress component is negligible (close to zero), hence the *biaxial stress state assumption* ($\sigma_{22} = 0$) which had to be used in the synchrotron data analysis is valid for current sample geometry.

In what follows, for more precise model validation, it is discussed the comparison of the predicted and measured residual stresses along the various measuring lines (**B**, **D**, **BD**) individually.

7.2.1. Comparison of predicted and measured residual stresses along D lines

The predicted residual strains and stresses along **D** lines are compared to the experimental neutron and synchrotron results in Fig. 7. Recall that the error bars shown on the measurement data is only the fitting error while the real error might be much larger due to the superposition of systematic errors, see Section 6. The predicted transverse (σ_{11}) residual stresses along **D2** line are in a very good agreement with both measured results, clearly showing an increase from the weld start–end towards the weld stop-end. Increase in the transverse (σ_{11}) stress along the weld centreline is an effect caused by the moving heat source. Only apparent deviation from the measurements is outside of the weld at position $Z = \pm 75$ mm, where the simulations falls roughly 50 MPa below the measured results. The longitudinal (σ_{33}) stress is over-predicted by less than 50 MPa in the weld region. Comparison of predictions along **D2** line with the neutron diffraction results is, however, not easy due to the scatter in the experimental data caused by the above mentioned grain size problems in the weld-metal region (see Section 6.1). Similarly, the comparison of the normal (σ_{22}) stress predictions with the experimental data is difficult because of the neutron diffraction data are very scattered and used synchrotron technique does not allow measurement of the through-thickness normal component (Martins et al., 2010). The predictions of transverse (σ_{11}) and longitudinal (σ_{33}) stresses for other **D** lines are in a very reasonable agreement with both measurement results with predicted stresses being slightly on the conservative side.

7.2.2. Comparison of predicted and measured residual stresses along B lines

The predicted residual strains and stresses along **B** lines are compared to the experimental neutron and synchrotron results in Fig. 8. The transverse (σ_{11}) stress and longitudinal (σ_{33}) stress along **B2** line seems to be well captured in the parent-metal region and on the conservative side in the weld-metal region. The transverse (σ_{11}) and longitudinal (σ_{33}) residual stresses along **B** line which does not cross weld-metal region are in an excellent agreement with the both measurement data sets. The normal stresses are scattered, though it is clear that they ware very low in magnitude as predicted by the current model.

7.2.3. Comparison of predicted and measured residual stresses along BD line

Comparison of the predicted results along **BD** line with the neutron and synchrotron measurements in Fig. 8(c) and (f) indicate that the predicted transverse (σ_{11}) stress is in an excellent agreement with both measurements, whereas the longitudinal (σ_{33}) stresses are over-predicted particularly in the upper part of the plate. First of all, the choice of the constitutive law is very important for the upper part of the plate because of the reversed yielding (compressive yielding occurs during heating and it is followed by tensile yielding during cooling) and the strong Bauschinger effect of the 316LN steel (Smith and Smith, 2009a). This is well handled by the use of the Lemaitre–Chaboche mixed hardening model (Chaboche, 2008; Smith et al., 2009a) in the current simulation. Additionally, the upper part of the plate contains the weld-parent metal boundary (1400 °C isotherm) as well as the 1300 °C isotherm (upper annealing temperature). It is, thus, believed that the discrepancy between the model and the measurements which occurs mainly in the weld-metal region is partly due to the lack of proper mechanical properties of the weld metal which appear to have lower yield[3] than parent metal. Nevertheless, it is clear from the present results that in this case the modeller can use the parent weld mechanical properties with proper constitutive hardening behaviour and achieve very good results, which are slightly conservative. Another issue is the handling of high temperature softening. Even the use of two-stage annealing leads to short wavelength fluctuations in stress in the lower two weld beads between 2.5 mm and 7.5 mm beneath the surface. These are probably unrealistic, but are much lower than would be obtained with a simple single annealing temperature.

[3] Choosing the correct mechanical properties for weld metal is difficult, because what is required is a material model that evolves from the unhardened just-deposited state through the thermo-mechanical load cycles imposed during the multi-pass welding to finish at the final state of weld metal in a muti-pass weldment. The authors believe that the model currently used (based on parent plate material) starts with its yield strength slightly too high, so longitudinal stresses on D2 in the final bead are over-predicted, but cyclically hardens to about the correct end state, so stresses on D5, basically within PASS.1, are approximately correct.

The lower part of the plate contains only the parent metal. This part of the plate does not undergo the reversed yielding, i.e. yielding occurs either in compression or tension, see Fig. 11 (**N5**, **N6**). As it has been discusses in Smith and Smith (2009a), the most important variable for this part of the plate is the heat input which seems to govern residual stresses. If the heat input is sufficiently high, the compressive yielding during heating part of the thermal cycle spreads to the back face of the plate (Fig. 11, **N6**). On the other hand, if the heat input is low the tensile yielding occurs on the back face during heating up. It is, thus, clear from Fig. 11 (**N6**) that in the first pass compressive yielding occurs on the back face of the plate leaving the transverse (σ_{11}) and longitudinal (σ_{33}) stresses in compression. It means that the heat input is sufficiently high for the given thickness of the plate (without the slot depth). This is changing with the second and third pass as the thickness of the plate in the weld region is increasing due to the added weld metal. From the final residual stress produced after the third pass in Fig. 8(f) it is clear that the back face goes into tension, this suggests that the heat input is not anymore sufficiently high during the third pass to allow tensile yielding on the back face during the heat up.

7.2.4. Comparison of predicted and measured shear strains

Using the synchrotron spiral slit method it was possible to measure shear strain, ε_{13}. From Fig. 10 is clear that the model captures the shear strain component reasonably well. The physical origin of the off-diagonal elements of the strain/stress tensor around the ends of the slot can be understood by simplifying a slot weld by splitting it into (i) a linear weld (middle part) and (ii) two partial spot welds at the both ends of the weld bead (see schematic drawing in Fig. 10). At the mid-length of the slot, the principal, Cartesian, axes would be expected to be directed along the length of the slot, transverse to the slot and normal to the plate. However, out from the end of the slot (the end resembles a portion of a spot weld) the principal axes are expected along radial and hoop directions relative to the spot as well as the plate normal direction. When these polar strains/stresses are resolved onto Cartesian axes the off-diagonal terms with the observed symmetry are naturally generated. This suggests a deviation of the principal axis in the plane from the principal sample axis at the start–end and stop-end of the weld.

8. Conclusion

The present work discusses comprehensive numerical analysis of the residual stress field associated with a three-pass slot weld in an AISI 316LN austenitic stainless steel plate (NeT TG4 which is fully characterised international benchmark specimen). The paper describes in detail performed modelling procedure, which made use of extensive manufacturing records that provide all the necessary information as well as material data to predict residual stresses in AISI 316LN welds.

The thermal transient solution is often a major source of uncertainty in numerical weld residual stress predictions. Hence, the present modelling work employed a dedicated welding heat source modelling tool to reduce the uncertainties in the thermal solution by calibrating ellipsoidal Gaussian volumetric heat sources against: (i) measured temperatures recorded using an array of 12 thermocouples, and (ii) macrostructural observation of fusion boundaries. The mechanical simulations used the mixed isotropic-kinematic (Lemaitre–Chaboche) material hardening model to produce the most representative material response to the cyclic thermo-mechanical loading of material during the welding process. It becomes clear from the present analysis that in the case of austenitic steels which tend to substantially cyclically harden in first 10 cycles, the appropriate handling of material response during the welding process is crucial in predicting final residual stress field associated with the weld.

Additionally, the current model utilises a two-stage annealing functionality which deals with the loss of strain-hardening (softening) at higher temperatures more appropriately than the commonly used single temperature annealing approximation. The current weld modelling procedure outlined in this paper is validated by measurement results utilising two independent diffraction techniques. The results show that this level of sophistication in modelling procedure is required in order to accurately capture behaviour in the weld metal and HAZ regions where large thermo-mechanical cycles occur during the welding process.

Acknowledgment

The authors gratefully acknowledge the help by Dr Maxim Avdeev with the neutron diffraction phase analysis conducted on the high resolution diffractometer ECHIDNA at the OPAL reactor in Australian Nuclear Science and Technology Organisation. This paper is published with permission from EDF Energy Generation Limited. Dr Mike Smith acknowledges a Royal Academy of Engineering Global Research Award.

References

ABAQUS, 2007. A novel approach to annealing using ABAQUS-behaviour with soft annealing.
ABAQUS, 2008. Standard User's Manual, Version 6.8, SIMULIA.
Brough, L.A., 1983. The effects of processing on delta ferrite measurement. Journal Materials for Energy Systems, American Society for Metals 5, 36–42.
Chaboche, J.L., 2008. A review of some plasticity and viscoplasticity constitutive theories. International Journal of Plasticity 24, 1642–1693.
Gilles, P., El-Ahmar, W., Jullien, J.-F., 2009. Robustness analyses of numerical simulation of fusion welding NeT – TG1 application: single weld-bead-on-plate. International Journal of Pressure Vessels and Piping 86, 3–12.
Hutchings, M.T., Withers, P.J., Holden, T.M., Lorentzen, T., 2005. Introduction of the Characterization of Residual Stresses by Neutron Diffraction. Taylor& Francis, London.
Keinänen, H., 1999. Isotropic-Kinematic Hardening Models, VORSAC(99)W0060, VTT Manufacturing Technology Report VALC663.
Kröner, E., 1958. Zeitschrift Für Physik 151, 504–518.
Lindgren, L.E., 2007. Computational Welding Mechancis: Thermomechancial and Microstructural Simulations. Woodhead Publishing Limited, Cambridge.
Liss, K.-D., Hunter, B., Hagen, M., Noakes, T., Kennedy, S., 2006. Echidna–the new high-resolution powder diffractometer being built at OPAL. Physica B: Condensed Matter, 1010–1012.
Martins, R.V., Honkimäki, 2003. Textures and Microstructures 35, 145–152.
Martins, R.V., Ohms, C., Decroos, K., 2010. Full 3D spatially resolved mapping of residual strain in a 316L austenitic stainless steel weld specimen. Materials Science and Engineering: A 527, 4779–4787.
Muránsky, O., Bendeich, P.J., Smith, M.C., Kirstein, O., Edwards, L., Holden, T.M., 2010. Analysis of residual stresses in three-pass slot weld (NeT – TG4): Finite element modelling & neutron diffraction, Proceedings of PVP2010, 2010 ASME Pressure Vessels and Piping Division Conference.
Schreyer, A., Clemens, H., 2008. Neutrons and Synchrotron Radiation in Engineering Materials Science.
Smith, R.M., 2009. FEAT-WMT: Weld-Modelling Tool User's Guide FEATPLUS lmitted Report FP/CR/0029/09.
Smith, M.C., Smith, A.C., 2009a. NeT bead-on-plate round robin: comparison of residual stress predictions and measurements. International Journal of Pressure Vessels and Piping 86, 79–95.
Smith, M.C., Smith, A.C., 2009b. NeT bead-on-plate round robin: comparison of transient thermal predictions and measurements. International Journal of Pressure Vessels and Piping 86, 96–109.
Smith, M.C., Nadri, B., Smith, A.C., Carr, D.G., Bendeich, P.J., Edwards, L., 2009a. Optimisation of mixed hardening material constitutive models for weld residual stress simulation using the NeT Task Group 1 single bead on plate benchmark problem. ASME PVP 2009, Prague PVP2009-77158.
Smith, M.C., Smith, A.C., Wimpory, R.C., Ohms, C., Nadri, B., Bouchard, P.J., 2009b. Optimising residual stress measurements and predictions in a welded benchmark specimen: a review of phase two of the NeT Task Group 1 single bead on plate round robin, ASME Pressure Vessel and Piping Division Conference, Prauge.

Truman, C.E., Smith, M.C., 2009. The NeT residual stress measurement and modelling round robin on a single weld bead-on-plate specimen. International Journal of Pressure Vessels and Piping 86, 1–2.

Vasudevan, M., Bhaduri, A.K., Raj, B., Prasad Rao, K., 2003. Delta ferrite prediction in stainless steel welds using neural network analysis and comparison with other prediction methods. Journal of Materials Processing Technology 142, 20–28.